Marine Geology 380 (2016) 163–173

Contents lists available at ScienceDirect

Marine Geology

journal homepage: www.elsevier.com/locate/margo

Sedimentation, stratigraphy and physical properties of sediment on the Juan de Fuca Ridge

K.M. Costa [a,b,*], J.F. McManus [a,b], B. Boulahanis [a,b], S.M. Carbotte [a], G. Winckler [a,b], P.J. Huybers [c], C.H. Langmuir [c]

[a] Lamont-Doherty Earth Observatory of Columbia University, Palisades, NY 10964, USA
[b] Department of Earth and Environmental Sciences, Columbia University, New York, NY 10027, USA
[c] Department of Earth and Planetary Sciences, Harvard University, Cambridge, MA 02138, USA

ARTICLE INFO

Article history:
Received 7 May 2016
Received in revised form 1 August 2016
Accepted 4 August 2016
Available online 6 August 2016

Keywords:
Juan de Fuca Ridge
Sedimentation rates
Sediment density
Oxygen isotope stratigraphy

ABSTRACT

Sedimentation near mid-ocean ridges may differ from pelagic sedimentation due to the influence of the ridges' rough topography on sediment deposition and transport. This study explores whether the near-ridge environment responds to glacial-interglacial changes in climate and oceanography. New benthic $\delta^{18}O$, radiocarbon, multi-sensor track, and physical property (sedimentation rates, density, magnetic susceptibility) data for seven cores on the Juan de Fuca Ridge provide multiple records covering the past 700,000 years of oceanographic history of the Northeast Pacific Ocean. Systematic variations in sediment density and coarse fraction correspond to glacial-interglacial cycles identified in benthic $\delta^{18}O$, and these observations may provide a framework for mapping the $\delta^{18}O$ chronostratigraphy via sediment density to other locations on the Juan de Fuca Ridge and beyond. Sedimentation rates generally range from 0.5 to 3 cm/kyr, with background pelagic sedimentation rates close to 1 cm/kyr. Variability in sedimentation rates close to the ridge likely reflects remobilization of sediment caused by the high relief of the ridge bathymetry. Sedimentation patterns primarily reflect divergence of sedimentation rates with distance from the ridge axis and glacial-interglacial variation in sedimentation that may reflect carbonate preservation cycles as well as preferential remobilization of fine material.

1. Introduction

Marine sediments are a storehouse of the geochemical, biological, and physical changes in the ocean over thousands to millions of years. Their archival utility is predicated on slowly settling sediment blanketing the submarine landscape to abyssal flatness, but rough topographic features like hills, seamounts, and ridges can distort flow fields and depositional dynamics of sediment on the seafloor (Dubois and Mitchell, 2012; Johnson and Johnson, 1970; Mitchell and Huthnance, 2013; Turnewitsch et al., 2013; von Stackelberg et al., 1979). Uneven topography can alternately deflect, accelerate, and decelerate bottom currents, generating a heterogeneous depositional environment over a wide range of spatial and temporal scales (Turnewitsch et al., 2013). Extensive two-dimensional topographic features, such as mid-ocean ridges and submarine canyons, exhibit prominent sediment mobilization and transport from bathymetric highs to lows, both by currents and by downslope gravitational flows. Acoustic profiling characterizes sediment distribution, thickness, and depositional processes in the modern near-ridge environments of the Mid-Atlantic Ridge and the East Pacific Rise (Ewing et al., 1964; Hauschild et al., 2003; Lister, 1976; Marks, 1981; Mitchell et al., 1998; Ruddiman, 1972), but how these depositional environments respond to glacial-interglacial variability is poorly constrained. The unique geochemical and biological microcosm of a mid-ocean ridge motivates investigation into the integrity of the sediment medium to record the evolution of the ridge system over time.

Ridge-influenced sedimentary regimes can be recorded in the physical properties of sediments (Turnewitsch et al., 2013), such as accumulation rate, density, and magnetic susceptibility. These physical properties respond to changes in the porosity, the density and geochemical composition of the grains (e.g., calcium carbonate, terrigenous silicate, hydrothermal metals), and the grain size and shape (Breitzke, 2006). Variability in the flow field geometry translates into lower sediment accumulation rates and coarser grains under fast flows and higher sediment accumulation rates and finer grains in more quiescent areas. These spatial patterns compound with temporal variability, such as glacial-interglacial cycles in carbonate preservation (Farrell and Prell, 1989), which can affect both the density and grain size of the sediment medium. This paper presents sedimentation rates, density, and magnetic susceptibility for a suite of seven cores covering almost 700,000 years of sedimentation on the Juan de Fuca Ridge. We aim to determine the major modes of sedimentation in the near-ridge environment and

* Corresponding author at: Lamont-Doherty Earth Observatory of Columbia University, Palisades, NY 10964, USA.
E-mail address: kcosta@ldeo.columbia.edu (K.M. Costa).

http://dx.doi.org/10.1016/j.margeo.2016.08.003
0025-3227/

explore how they may have varied with climatic and oceanographic changes associated with glacial-interglacial cycles.

2. Study site & oceanography

The Juan de Fuca Ridge (JdFR) is located in the Northeast Pacific Ocean about 500 km off the coast of North America in the subpolar transition zone, where warm surface waters from the west wind drift diverge into the California Current, flowing south, and into the Alaskan Gyre, flowing north (Hickey, 1979). Bottom waters in the vicinity of the JdFR are composed of Pacific Deep Water (Macdonald et al., 2009) (Fig. 1), which constitutes the oldest and most corrosive deepwater in the modern ocean (Key et al., 2002; Kroopnick, 1985). Because corrosivity of deep Pacific waters leads to poor carbonate preservation (e.g., Karlin et al., 1992), paleoceanographic investigations into this region have been limited by low sedimentation rates and difficulties generating age models via foraminiferal stable isotope stratigraphy. Thus the relatively shallow sedimentary environment on the JdFR (<3000 m), which rises above the corrosive bottom waters, may provide important information about ocean circulation and chemistry in this understudied region.

The JdFR is an intermediate spreading ridge (56 mm/yr) that is characterized by extensive hydrothermal activity and hot spot volcanism (Karsten and Delaney, 1989; Massoth et al., 1994; Normark et al., 1983; Wilson, 1993). The Cleft Segment of the JdFR is located at the southern end of the ridge system, bounded by the Vance Segment to the north and the Blanco Fracture Zone to the south. The Cleft Segment is 55 km long and contains a modest axial rift that is 50–150 m deep and 2–4 km wide (Baker et al., 1989; Carbotte et al., 2006). Hydrothermal activity occurs within the rift valley both as diffuse venting, along the southern 18 km of the segment, and as discrete venting, via Pipe Organ, Monolith, and Fountain vents at the north end of the segment (Massoth et al., 1994). Outside the rift valley is a thinly sedimented axial plateau with low relief abyssal hills that extends approximately 16 km from the ridge axis and terminates in a 300 m scarp before continuing into regularly spaced, ridge-parallel crests and troughs further on the ridge flanks (Carbotte et al., 2008, 2006). Whereas the western flanks contain the preponderance of seamounts and hotspot activity (Davis and Karsten, 1986), the eastern flanks suffer from frequent turbidity current activity off the coast of North America (e.g., Goldfinger et al., 2012; Horn et al., 1971). Turbidity currents interrupt and sometimes erode hemipelagic sedimentation and interfere with sedimentological reconstructions of glacial-interglacial climate change, so that the spatial and temporal variability in sedimentation in this region is poorly constrained. To minimize the influence of turbidity currents, this study focuses on cores that were collected from the western flanks of the Cleft Segment on the SeaVOICE cruise (AT26-19) of the R/V Atlantis in September 2014 (Table 1).

During the cruise, over 50 m of sediment was collected on the JdFR flanks, in addition to basalt rock cores and high-resolution multi-beam sonar mapping. This paper focuses on the longest, stratigraphically-intact records of six piston cores (05PC, 09PC, 12PC, 20PC, 35PC, 38PC) and one "Big Bertha" gravity core (39BB). Bathymetric highs were targeted for coring sites to maximize carbonate preservation, and so cores were recovered from a limited depth range (2655–2794 m) along the crests of ridge-parallel abyssal hills. This coring strategy resulted in both ridge-perpendicular transects as well as ridge-parallel transects along basement isochrons, based on geomagnetic reversals

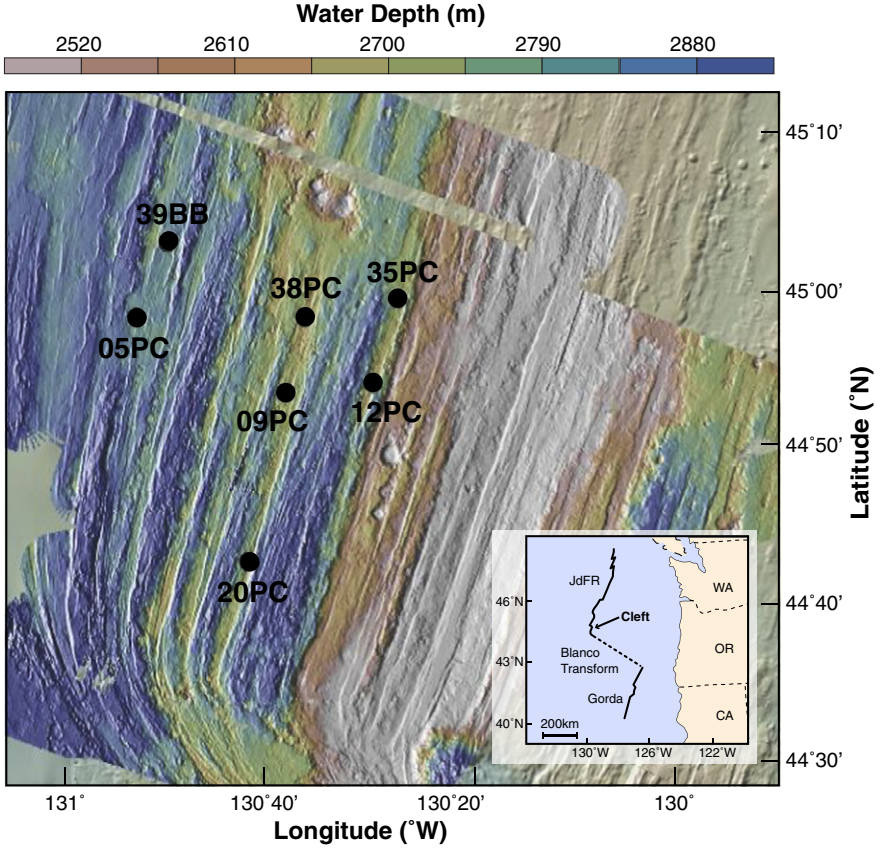

Fig. 1. Map of the study region. Location of the Cleft Segment of the Juan de Fuca Ridge relative to the North American coast. Bathymetric map of the Cleft Segment generated by shipboard multibeam data. The ridge can be identified as the NE-SW trending bathymetric high (in white). AT26-19 core locations on the western flanks of the ridge are shown with black circles, and locations are provided in Table 1. All cores were recovered from the crests of abyssal hills in order to obtain sediments with adequate carbonate preservation to generate age models. Cores 12PC and 35PC are both located next to the scarp that defines the boundary of the poorly sedimented axial plateau. (Inset) Location of the Cleft Segment of the Juan de Fuca Ridge relative to the North American coast.

Table 1
AT26-19 cores included in this study.

Core	Lat (°N)	Long (°W)	Water depth (m)	Core length (cm)
05PC	44.97283	130.87850	2711	644.7
09PC	44.88717	130.63683	2678	765.9
12PC	44.89750	130.50433	2689	550.2
38PC	44.97053	130.60653	2655	736.1
20PC	44.70817	130.70383	2738	540.5
35PC	44.99118	130.45737	2731	642.4
39BB	45.04507	130.83318	2794	513.0

and spreading rates from the ridge crest (Wilson, 1993). Cores 05PC and 39BB are located on the oldest crust (~1.8 million years old), while cores 38PC, 09PC, and 20PC are located on intermediate age crust (1.0 million years old). Cores 35PC and 12PC are located on the youngest crust (700,000 years old), and core 12PC impacted basalt at its base.

3. Methods

3.1. $\delta^{18}O$ stratigraphy

Samples from four cores (05PC, 09PC, 12PC, and 38PC) were analyzed for $\delta^{18}O$ in order to establish baseline chronologies. Samples were freeze-dried, and then an aliquot was weighed into a 125 mL Nalgene bottle, filled with approximately 100 mL of tap water, and disaggregated on a tumble wheel for 2 h. Samples were then sieved at 63 μm, and a soft brush was used to gently break up clay clumps that did not sufficiently disintegrate during tumbling. The coarse sediment fraction remaining in the sieve was then dried and weighed, and the mass fraction of coarse material was calculated relative to the initial aliquot mass. *Uvigerina* sp. tests were picked from the coarse fraction and analyzed at Lamont Doherty Earth Observatory (LDEO) on a Thermo Delta V Plus equipped with a Kiel IV individual acid bath device. Samples have been replicated at >20% frequency and standardized to NBS-19. All data are reported on the VPDB scale with precision ≤0.05‰. Samples from 20PC, 35PC, and 39BB were also sieved for coarse fraction, as described above.

3.2. Radiocarbon

Coretop radiocarbon dates for 05PC, 09PC, 12PC, and 38PC were analyzed on *Globigerinoides bulloides*. Samples were picked from the shallowest depth at which sufficient foraminifera tests were available for analysis, as shallow as 0 cm depth (38PC) and as deep as 16 cm depth (09PC). Analyses were performed at the National Ocean Sciences Accelerator Mass Spectrometry Facility at Woods Hole Oceanographic Institution. Radiocarbon ages were calibrated to calendar years using Calib 7.0 Marine13 (Reimer et al., 2013; Stuiver and Reimer, 1993) with a total reservoir correction of 800 years ($\Delta R = 400$).

3.3. Multi-sensor track data

Bulk sediment physical properties were measured shipboard on a Geotek multi-sensor track (MST) system at 1 cm resolution. Gamma ray attenuation is inversely dependent on the mass of sediment within a given volume (Gunn and Best, 1998), and it can be calibrated to density through discrete sample analyses. Volume-controlled samples were taken from select cores by depressing standard paleomagnetic sample boxes ($2 \times 2 \times 2$ cm) into the sediment, concentrated at the top of each core (5 cm, 25 cm, 50 cm, and every 50 cm thereafter) in order to constrain the density differences associated with high coretop porosity. Only those boxes that extracted the full 8 cm^3 volume were included in further analysis. Boxes were parafilmed and refrigerated to avoid evaporation during transport back to LDEO, where they were weighed before and after freeze-drying to obtain the wet and dry sample masses. A salt correction was applied assuming S = 35‰ and using the calculated mass of seawater lost. Wet and dry bulk densities could then be calculated using the known 8 cm^3 sample volume.

In addition to density, magnetic susceptibility (MS) was also analyzed on the Geotek multi-sensor track system. MS measures how easily a substance can be magnetized, and it is quantified as the magnetization induced by applying a magnetic field to a specific volume of material (Gunn and Best, 1998). The magnetic field is generated by a whole core loop sensor (diameter 14 cm) that integrates over 12 cm of the core. The MS of bulk sediment is a function of the concentration and type of magnetizable minerals within the induced magnetic field (Carmichael, 1982). The major mineral phases in marine sediment, such as quartz and calcite, are diamagnetic and exhibit no magnetism. Instead, the MS of bulk sediment reflects the concentration of trace minerals, such as clays (nontronite, montmorillonite, biotite) and Fe-rich phases (siderite, hematite, pyrite, magnetite), which exhibit magnetism within (and sometimes without) a magnetic field. Clays and Fe-rich phases characterize terrigenous sediment, and so MS is often a proxy for terrigenous sediment inputs (Bloemendal and deMenocal, 1989; deMenocal et al., 1991; Larrasoaña et al., 2008).

3.4. Age model generation

Age models were created by incorporating the temporal information in the coherent MST data with the benthic $\delta^{18}O$ records. Initial age models for 05PC, 09PC, 12PC, and 38PC were generated by graphic correlation (Prell et al., 1986) of the individual $\delta^{18}O$ records to the global benthic stack (Lisiecki and Raymo, 2005), and radiocarbon-based ages were used to constrain the coretop ages (Table 2). Age models were subsequently adjusted to align prominent features in the MST data. A full description of the age model procedure is presented in the Supplementary Materials.

4. Results

Oxygen isotope records for 05PC, 09PC, 12PC, and 38PC are presented in Fig. 2. The $\delta^{18}O$ records largely correspond with the global benthic stack (Lisiecki and Raymo, 2005), with relatively enriched glacial periods ($\delta^{18}O \geq 4.5‰$) and relatively depleted interglacial periods ($\delta^{18}O \leq 4.0‰$), reflecting the dominant influence of global ice volume. The amplitude of these cycles is somewhat muted, which may be attributed in part to the smoothing influence of bioturbation. However, isotope cycles from low sedimentation rate portions of, e.g., 09PC, show no further diminishing in the isotope range of glacial cycles (Marine Isotope Stage 9-10-11-12, or MIS9-10-11-12) despite the expectation for an enhanced bioturbation effect. One possible influence on the isotopic records may be the smaller glacial-interglacial temperature changes of approximately 2 °C in the deep Pacific relative to those of ~4–5 °C in the Atlantic (Chappell and Shackleton, 1986; Labeyrie et al., 1987; Schrag et al., 1996), which are heavily represented in the cores used for the global benthic stack (Lisiecki and Raymo, 2005). Regardless, the glacial-interglacial cycles are sufficiently identifiable for the purposes of constructing preliminary age models (see Supplementary Materials). Coretops for 12PC (~19.2 ka) and 38PC (~16.6 ka) only reach the last deglaciation, indicating no recovery of Holocene sediment at these sites. Slightly deeper samples from 05PC (~15.1 ka) and 09PC (13.7 ka) project to early Holocene ages at the respective coretops.

Table 2
Radiocarbon ages.

Core	Depth (cm)	NOSAMS accession #	^{14}C age (years)	±	Calendar age (years)	±
05PC	8	OS-118739	15,050	65	15,399	208
09PC	16	OS-118740	13,700	50	13,447	227
12PC	1	OS-118741	18,300	95	19,185	317
38PC	0	OS-118613	16,100	40	16,625	131

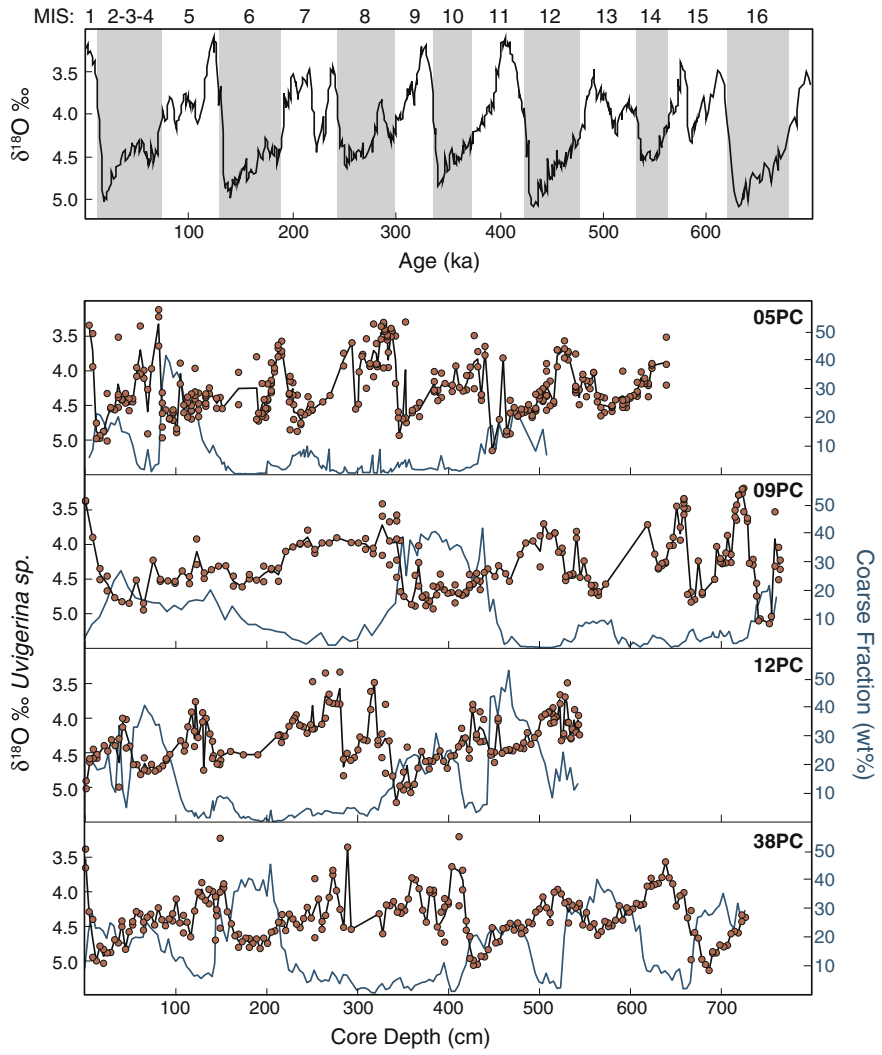

Fig. 2. Oxygen isotope stratigraphies for 05PC, 09PC, 12PC, and 38PC. (*Top*) Target benthic $\delta^{18}O$ stratigraphy based on the global stack (Lisiecki and Raymo, 2005). Marine Isotope Stages (MIS) are identified at the top. Glacial periods (even MIS) are highlighted in gray bands, after Martinson et al. (1987). (*Bottom*) Oxygen isotope data are reported on the VPDB scale with precision ≤0.05‰, and all replicates of individual samples are included (red circles). Black lines pass through the average isotopic value for each sample. Intra-sample variability tends to be greater during interglacial than glacial periods, potentially reflecting bioturbation across abrupt isotopic changes. Coarse fraction is shown in blue and tends to increase during glacial periods, when carbonate preservation is enhanced.

Raw MST data for all seven cores are presented in Supplemental Figure 1. The relationship between gamma attenuation and density appears consistent across multiple cores (Supplemental Figure 2), and so one density calibration, using simple least squares and a linear fit, was applied to all cores. The calibrated records (Fig. 3) indicate clearly defined cycles in dry bulk density (DBD) on the JdFR. The sediment appears to fluctuate between two steady states: high density periods with DBD ≈ 0.7 g/cm^3 and low density periods with DBD ≈ 0.4 g/cm^3, and the transitions between these periods appear relatively abrupt.

Unlike the DBD, the magnetic susceptibility (MS) records generally show low amplitude variability and have gradual transitions, which are likely derived from the smoothing effects of the MS measurement. The most prominent feature is a peak, approximately five times the amplitude of background levels, that occurs ~272 ka before the last three DBD cycles. MS is otherwise low, showing a generally inverse relationship with DBD and ranging from 10 to $15 * 10^{-6}$ in high density periods to $30–40 * 10^{-6}$ during low density periods (Fig. 3).

The coarse fraction (mass percent >63 μm) positively correlates with density and tends to increase during high density periods, reaching a maximum of 52.7 wt% in 12PC (Fig. 3). Average coarse fractions during a high density period are comparable (30–40 wt%) for 09PC, 12PC, 20PC, 35PC, 38PC, and 39BB, while 05PC often exhibits lower coarse fraction (20 wt%). Low coarse fractions (<5 wt%) are typical of low density periods, and near-zero coarse fractions characterize the sediment associated with the MS peak. Visual inspection of coarse material indicates that it is predominantly composed of planktonic foraminifera (*G. bulloides*, *N. pachyderma*) with occasional basalt, quartz, and mica chips.

5. Discussion

5.1. Physical properties

The consistent patterns of DBD, $\delta^{18}O$, magnetic susceptibility, and coarse fraction records from the cores permitted the extraction of a regional signal in the physical properties. The individual records were averaged into stacks (Fig. 4), and the stacked records demonstrate the predictable effects of the climatic and oceanographic variability associated with glacial-interglacial cycles on the physical properties of sediments. Glacial periods are characterized by high density, low magnetic susceptibility, and high coarse fraction, while interglacial periods are characterized by low density, high magnetic susceptibility, and low coarse fraction. Dry bulk density has previously been shown to correlate with carbonate content (Mayer, 1991, 1979), and changes in carbonate

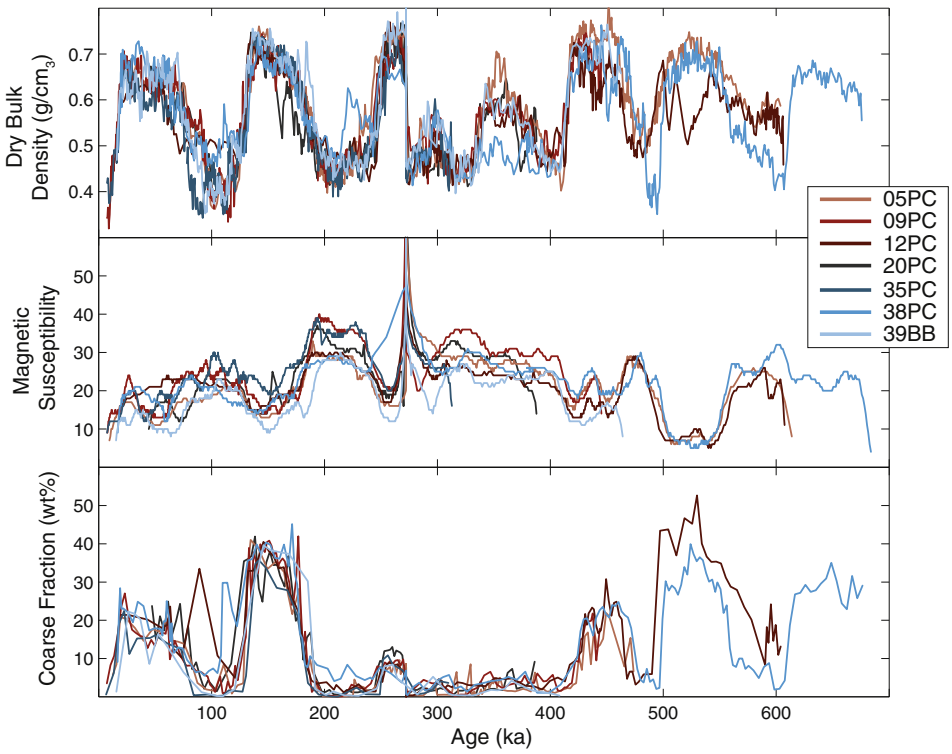

Fig. 3. Density, magnetic susceptibility, and coarse fraction records from all seven cores. Colour legend is the same in all three panels. Agreement between the cores is within the error of the calculation (±10%) for dry bulk density (see, e.g., Supplemental Figure 2). Low count rates for magnetic susceptibility would lead to large errors (±20%) that could account for the more variable inter-core comparison. Reproducibility of coarse fraction measurements (±10%) could also account for the general range of values, although spikes in coarse fraction, e.g. in 12PC ~90 ka, likely reflect real features, in this case a bioturbation channel.

preservation could explain the temporal variability in physical properties. High carbonate preservation during glacial periods increases the sediment density and dilutes the MS, and the opposite occurs during interglacial periods. Partial dissolution weakens the integrity of the foraminifera tests and increases the degree of fragmentation (Berger, 1979), reducing the mass fraction of coarse material during interglacial periods. However, the glacial-interglacial cycles in carbonate preservation are inadequate to explain the anomalous peak in MS around 272 ka. This peak corresponds with near-zero coarse fraction and relatively high density, equal to or slightly greater than the glacial average, and it indicates an extreme depositional event of 10 s to 100 s of centimeters of dense, fine and highly magnetizable material. The sediment is unique in the history of the JdFR, and it is bounded by a sharp base and bioturbation at the top. Deposition persists on the regional scale, not just on the flanks of the JdFR, but as far west as Cobb Square, where a similarly high MS event has been recorded in the same stratigraphic position (Karlin et al., 1992). The sedimentological characteristics and the severe and widespread nature of this event are an intriguing puzzle that certainly warrants further investigation, although it is beyond the scope of this paper.

5.2. Near-ridge sedimentation environment

Sedimentation rates are highly variable on the JdFR both spatially and temporally. Overall, sedimentation rates range between 0.25 and 3.18 cm/kyr (Fig. 5), and this range is captured within single cores with variable sedimentation rates over time (35PC: 0.41 cm/kyr in MIS9 vs 3.18 cm/kyr in MIS5) and between cores during the same time slice (MIS5: 0.61 cm/kyr at 05PC vs 3.18 cm/kyr at 35PC). Comparable sedimentation variability has been observed in the near-ridge environment on the East Pacific Rise, Galapagos Spreading Center, and Southeast Indian Ridge (Mitchell, 1998, 1993), where sedimentation rates can vary by as much as 80%. All cores on the JdFR show an increase in sedimentation rates during the MIS8 interval that contains the MS peak at 272ka, but otherwise no consistent glacial-interglacial response is apparent in all cores. Some cores generally show higher sedimentation rates during glacial periods (05PC, 12PC, 20PC, 38PC) while others show higher sedimentation rates during interglacial periods (09PC, 35PC, 39BB).

Sediment accumulation in the near ridge environment is primarily controlled by three factors: vertical rain rate of pelagic sediment, degree of carbonate dissolution, and intensity of sediment redistribution along the seafloor (Hauschild et al., 2003). Because surface productivity is relatively stable at the regional scale (tens of kilometers), the pelagic rain rate is likely to be homogeneous across the seven cores on the JdFR. Bathymetry deepens with increasing distance from the ridge, and so carbonate dissolution may similarly increase as the core sites enter more corrosive bottom waters. Increased dissolution at deeper sites would reduce the sedimentation rates there, but the cores included in this study represent a relatively narrow depth range (2655–2794 m), so that changes in carbonate preservation are unlikely to explain much of the heterogeneity between cores. Alternatively, sediment redistribution on the seafloor can generate locally high and low sedimentation rates by gravitational slumping, resuspension, and transport in bottom currents. Sediment redistribution is ubiquitous in the modern ocean (Francois et al., 2004), but mid-ocean ridges may present the most extreme example, in which deep pockets of sediment surround regions of nearly bare rock (e.g. Ewing et al., 1964). The spatially heterogeneous sedimentation on the JdFR evident from our cores suggests that sediment redistribution may be the dominant control on sedimentation rate in this region.

To assess the major modes of sedimentation, an empirical orthogonal function (EOF) analysis was conducted on the sedimentation rates for the time periods covered by all seven cores (MIS2-7). The

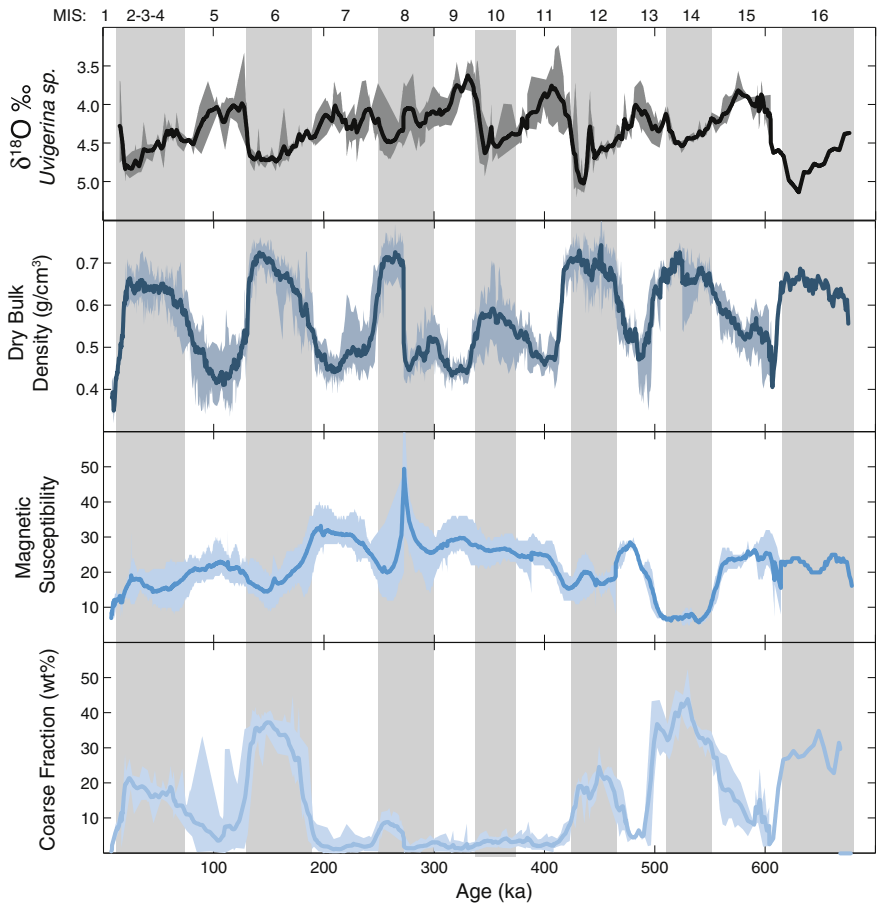

Fig. 4. Stacked oxygen isotope, density, magnetic susceptibility, and coarse fraction records. Individual records from all seven cores were interpolated onto 0.1 kyr timesteps and averaged at each timestep to generate the stacked records. Gray bars are as in Fig. 2. Shaded envelopes show the full range of values averaged within each timestep.

sedimentation rates were normalized (z-scored) to place them all on the same amplitude scale before analyzing for the major modes and loading factors for each core. The analysis identified two major modes of deposition (Fig. 6). The first mode explains 61.2% of the variance in sedimentation rates and comprises a divergence in sedimentation rates over time. It is particularly prominent at 09PC (positive

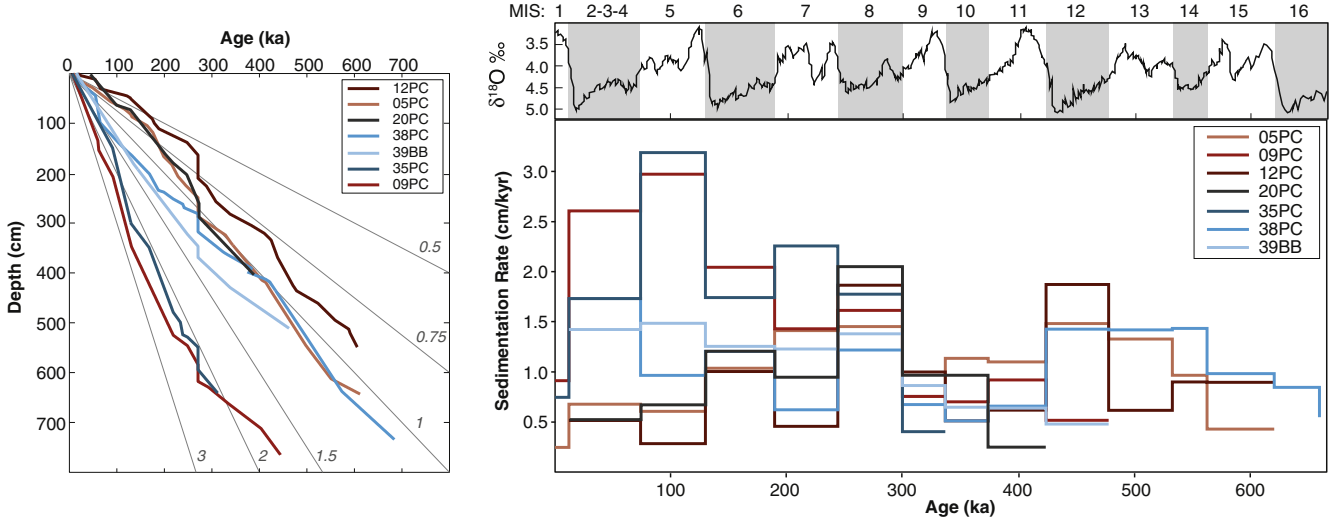

Fig. 5. Temporal variability in sedimentation rates. (*Left*) Age models for all seven cores. Gray reference lines indicate age vs depth for stable sedimentation rates from 0.5 to 3 cm/kyr. Sedimentation rates for the JdFR cores generally fall within this range. 09PC and 35PC have the highest sedimentation rates, while 12PC has the lowest sedimentation rate.(*Right*, *top panel*) Global benthic $\delta^{18}O$ stack (Lisiecki and Raymo, 2005). Marine Isotope Stages (MIS) are identified at the top, and glacial periods (even MIS) are highlighted in gray bands, as in Figs. 2 and 4. (*Right*, *bottom panel*) Sedimentation rates averaged over glacial-interglacial time slices. Several cores show glacial-interglacial cycling in sedimentation rates, with 12PC showing higher sedimentation rates during glacial periods and 35PC showing higher sedimentation rates during interglacial periods.

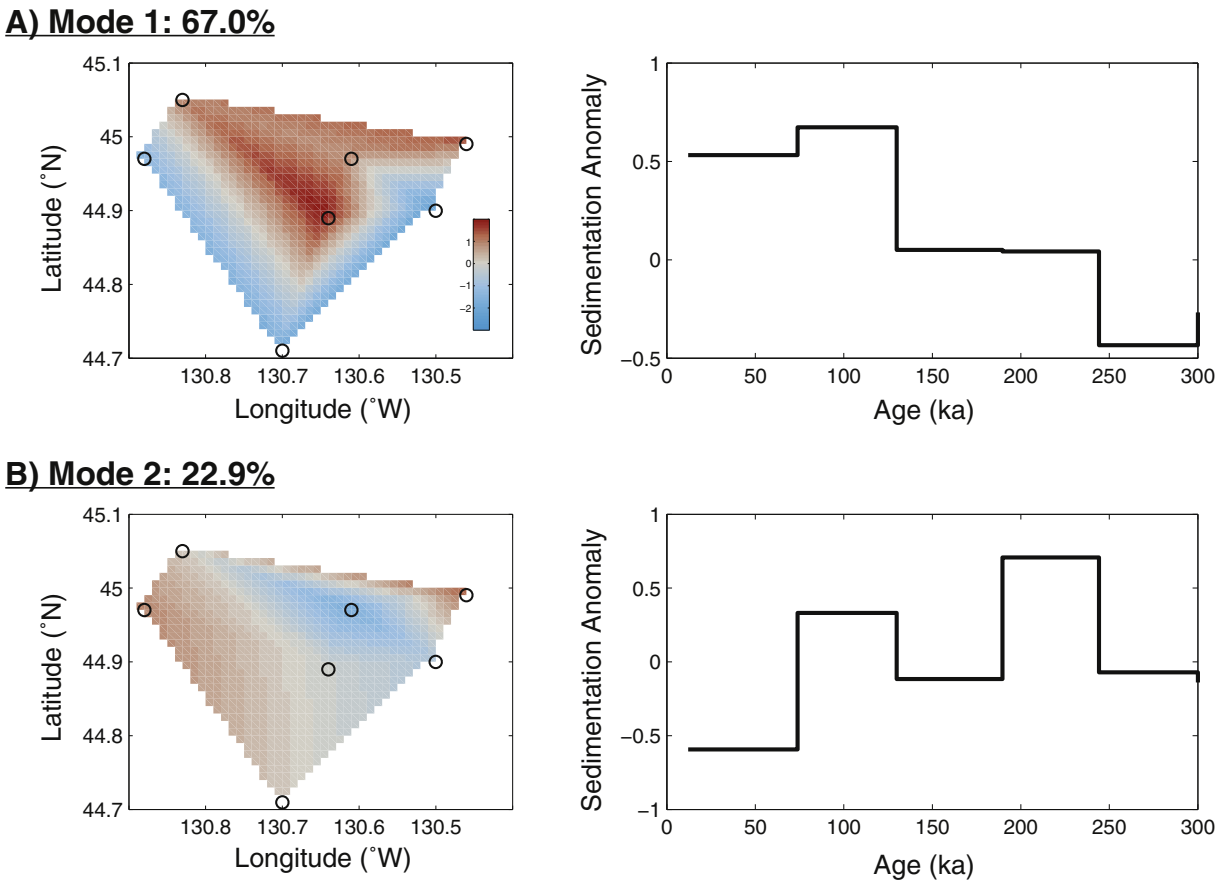

Fig. 6. Empirical orthogonal function (EOF) analysis of the spatial variability in sedimentation rates. Left panels show the factor loading on each core interpolated across the region. Colourbar is shown in the top panel for both modes, with red indicating a positive loading of the mode and blue indicating a negative loading of the mode. Right panels show the principal component that reflects the sedimentation anomaly over time. The first mode of sedimentation, divergence in sedimentation rates over time, accounts for 61.2% of the variance in sedimentation rates, and it is particularly important for cores 09PC and 12PC. The second mode of sedimentation, glacial-interglacial variation, accounts for 25.4% of the variance in sedimentation rates, and it is particularly important for core 38PC.

correlation) and 12PC (negative correlation). The second mode explains 25.4% of the variance in sedimentation rates and consists of glacial-interglacial variation in sedimentation rates. It is particularly important at 38PC (negative correlation) and 05PC (positive correlation).

5.2.1. Mode 1 sedimentation pattern: divergence of sedimentation rates over time

Diverging sedimentation rates over time correspond with increasing distance from the ridge, with positive loadings indicating increasing sedimentation rates over time (09PC, 38PC, 35PC, 39BB) and negative loadings indicating decreasing sedimentation rates over time (12PC, 20PC, 05PC). Locally variable sedimentation in the near-ridge environment is expected because 1) the bathymetry of sparsely sedimented newly formed seafloor is rougher, 2) tidal dissipation increases near rough bathymetry, 3) bottom currents are faster and likely to interact with the elevated seafloor, 4) active tectonic faulting associated with the formation of abyssal hills may be ongoing, 5) micro-earthquakes may contribute to small-scale sediment mobility, and 6) faults bounding abyssal hills are steeper having undergone less tectonic erosion. The biggest contributing factor for sediment redistribution in the study area is the steep relief of the JdFR (Mitchell, 1995; Mitchell et al., 1998; Webb and Jordan, 2001), which is largely created as result of extensional faulting. Sediment redistribution from bathymetric highs to bathymetric lows occurs as localized downslope movements (Mitchell et al., 1998; Ruddiman, 1972; van Andel and Komar, 1969), which but often proceed as a gentle and semi-continuous flow but can also occur as abrupt and episodic slumps (Heezen and Rawson, 1977; Marks, 1981). Sediments develop cohesiveness that limits remobilization as they age, and thus sediment added through lateral remobilization, particularly by gentle gravity flows, is likely to be quasi-contemporaneous to surface-derived sediment. Such persistent small-scale lateral sedimentation is consistent with the dry bulk density and MS records of the study cores, which contain few sharp transitions diagnostic of slumps or other rapid shifts in sedimentation.

The individual bathymetric setting for each study core suggests that local relief does play a role in controlling the sedimentation rates. Although all cores are located on or near the tops of abyssal hills, these features vary in relief along strike with local saddle points along their crest as well as longer wavelength deepening towards the ends of these hills (Figs. 1 and 7). Core 12PC is located adjacent to a steep vertical scarp of nearly 200 m (Fig. 1, Supplemental Figure 3c, Supplemental Figure 4), and downslope transport away from the core site may explain the generally low sedimentation rates observed there. Core 35PC, on the other hand, with high average sedimentation rates, is situated in a relatively flat bathymetric low region near the end of this same abyssal hill that may readily accumulate sediment transported, for example, from the nearby axial plateau. Similarly, core 09PC, also located in a local broad bathymetric low, has high average sedimentation rates. Of the other cores, all with similar moderate average sedimentation rates, one is sited in a local bathymetric low (core 39BB) and three are located on local highs (05PC, 38PC, 20PC).

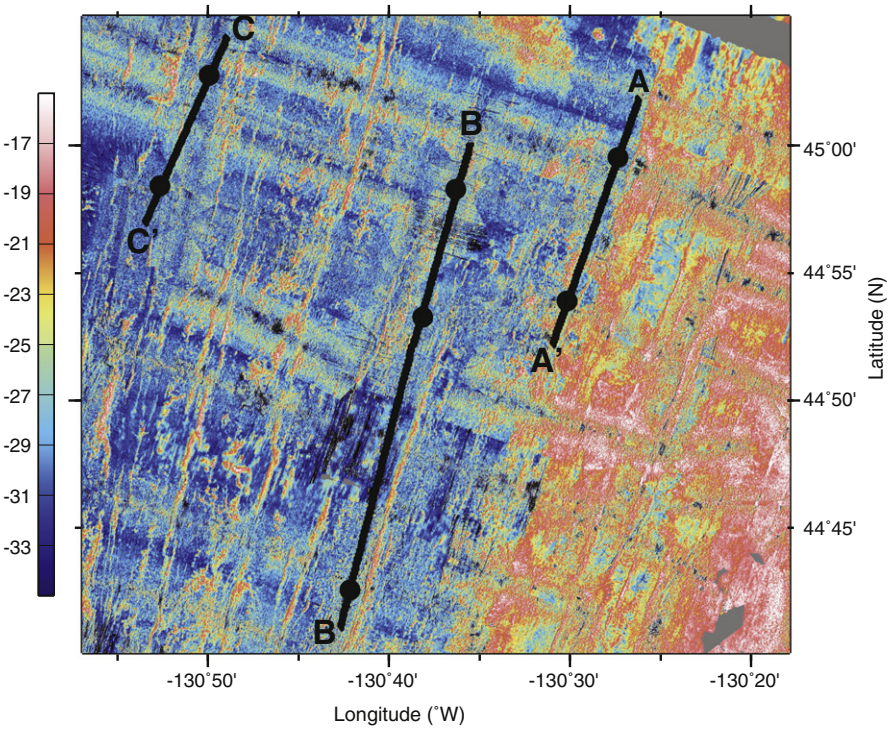
C
C'
B
B'
A
A'
-17
-19
-21
-23
-25
-27
-29
-31
-33
45˚00'
44˚55'
44˚50'
44˚45'
Latitude (N)
-130˚50'
-130˚40'
-130˚30'
-130˚20'
Longitude (˚W)

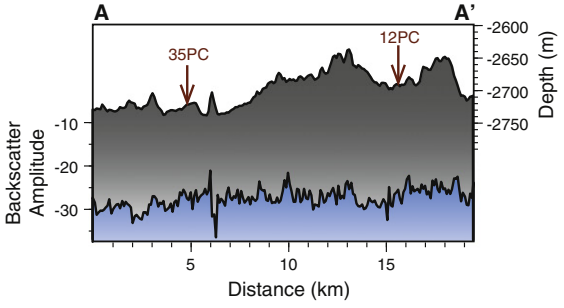
A
A'
35PC
12PC
-2600
-2650
-2700
-2750
Depth (m)
-10
-20
-30
Backscatter Amplitude
5
10
15
Distance (km)

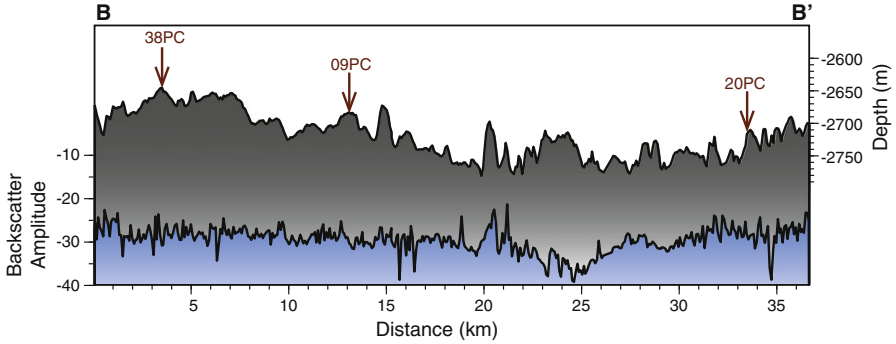
B
B'
38PC
09PC
20PC
-2600
-2650
-2700
-2750
Depth (m)
-10
-20
-30
-40
Backscatter Amplitude
5
10
15
20
25
30
35
Distance (km)

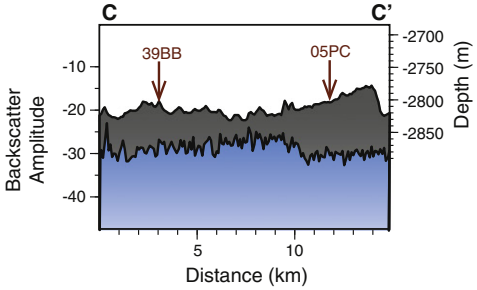
C
C'
39BB
05PC
-2700
-2750
-2800
-2850
Depth (m)
-10
-20
-30
-40
Backscatter Amplitude
5
10
Distance (km)

Although the interpretation of sediment cover in the 3.5 kHz subbottom profiler data acquired at the core sites (Supplemental Figure 3) was complicated by side echoes associated with the rough seafloor topography and the short wavelength of variations in abyssal hill relief, simultaneous seismic backscatter amplitude mapping supports the inference of heterogeneous sediment deposition in the near-ridge environment (Fig. 7). Backscatter amplitude varies with fine-scale roughness of the seafloor, with gradually decreasing backscatter strength with distance from the ridge as the crust ages and accumulates sediment (Mitchell, 1993). In our study area, the high backscatter associated with the broad axial plateau at Cleft Segment and lower backscatter of the older crust at our cores is overprinted by narrow linear zones of high backscatter, associated with large fault scarps, as well as more sinuous bands of higher backscatter, which mark the edges of volcanic flow fronts. Away from these zones of high backscatter/steeper topography, small regional variations in backscatter amplitude above the sonar beam noise are consistent with the variability in sedimentation rates found in individual cores (Fig. 7). For example, the low sediment rate core 12PC is located near an area of higher backscatter than at core 35PC, although both are sited in similar age crust. However, along the 1.8 Ma transect, core 05PC is located in a region of lower backscatter but has similar average sedimentation rates as 39BB. The lack of a correlation between acoustic backscatter and sedimentation patterns along the older transects likely reflects the limited sensitivity of these data to sediment thicknesses >5–10 m given the acoustic penetration of the 12 kHz sonar used (e.g., Mitchell, 1993).

In addition to gravity flows and slumping from steep bathymetry, sediment redistribution along the seafloor due to bottom currents may also contribute to the sedimentation patterns. Sediment redistribution can occur anywhere bottom currents are strong enough to resuspend and laterally transport sediments in nepheloid layers on the seafloor (Francois et al., 2004). On mid-ocean ridges, these currents are predominantly tidal (Polzin, 1997; Thurnherr and Speer, 2003), which supply 40–50% of the kinetic energy (Thomson et al., 2003; Thurnherr et al., 2005) and generate enhanced diapycnal mixing over the rough topography (Polzin, 1997). Bathymetric features like seamounts and ridge parallel abyssal hills amplify tidal currents and create complex flow fields that can extend up to 10 km from the feature (Turnewitsch et al., 2008, 2004). Transient currents as fast as 10 cm/s due to tidal forcing have been documented on the nearby Endeavor Segment of the JdFR (Thomson et al., 2003). Such currents are capable of transporting fine particles, particularly phytodetritus and other biogenic material (Beaulieu, 2002), and especially in regions with high relief (Kienast et al., 2007; Lonsdale et al., 1972), although they are unlikely to entrain coarse particles, such as foraminifera and volcanic ash (Marcantonio et al., 2014).

Sediment on the JdFR is predominantly fine, averaging just 12% coarse, and fluctuating between 0 and 5% coarse (interglacial periods) to 30–40% coarse (glacial periods). In the near ridge environment, this fine material can easily be remobilized by a wide range of influences, including tidal currents generated by the steep topography, near-ridge jets, shaking by micro-earthquakes, and bioturbation by macrofauna. This redistribution would result in low sedimentation rates at coarse lag deposits and high sedimentation rates at focused sediment deposition banks. Farther from the ridge, the subdued topography damps the tidal intensity, so that fine material is more likely to settle vertically to the seafloor, resulting in higher sedimentation rates. Thus the divergence in sedimentation rates over time likely reflects the migration of the core sites out of the variable current zone of the ridge crest into the more quiescent waters of the ridge flanks.

5.2.2. Mode 2 sedimentation pattern: glacial-interglacial variation of sedimentation rate

A secondary glacial-interglacial cycle of sedimentation rates is weakly present at some of the core sites. Consistently variable sedimentation rates might be expected, given the cyclical calcium carbonate preservation in the Pacific Ocean that peaks during glacial intervals (Farrell and Prell, 1989). Accumulation rates in some of the study cores do vary in this way, yet others (5PC, 35PC) display the opposite pattern, suggesting an important additional influence of lateral redeposition. Because the stratigraphic indices of $\delta^{18}O$ and physical properties remain coherent, this sediment redistribution is likely to have occurred nearly syndepositonally and over relatively small spatial scales.

Sedimentary characteristics such as grain size and composition may have contributed to this cyclical redistribution. The sediment at all study sites is predominantly fine during interglacial periods because 1) poor carbonate preservation increases the degree of fragmentation of large foraminiferal tests into fine pieces, 2) reduced surface stratification in the North Pacific generally increases interglacial productivity in this region (Galbraith et al., 2008; Jaccard et al., 2005; Lam et al., 2013) thus increasing the fraction of fine phytodetritus, 3) the lack of coarse particles reduces sediment cohesion that would otherwise facilitate resistance to remobilization (Mitchener and Torfs, 1996). These effects combine to form a more easily mobilized sediment substrate during interglacial periods, allowing sediment to pond by moving from local highs to nearby depressions in a process that would eventually contribute to the observed smoothing of the seafloor away from the ridge. Tidal currents (e.g., Lavelle and Cannon, 2001), ridge-associated jets (Lavelle, 2012), shaking from micro-earthquakes, and bioturbation by macrofauna could all contribute to resuspension that subsequently focuses sediment deposition into thick sediment ponds, resulting in high sedimentation rates for some sites (e.g., 05PC, 35PC) and low sedimentation rates in the sediment source regions.

Although it may be less likely, it is also possible that the relatively high sedimentation rates during interglacial periods could instead be related to increased erosion in the near-ridge environment during glacial periods. Lower sea level would result in a greater fraction of tidal dissipation over relatively rough bathymetry in the deep ocean rather than on the continental shelves (Egbert et al., 2004). This increase in tidal energy might increase winnowing of fine sediment during glacial periods, providing an alternative explanation for the coarser grain size during glacial intervals and relatively higher sedimentation rates in interglacial intervals observed at some study sites. Future investigation using ^{230}Th systematics and focusing factors may provide insights into the relative changes in focusing and winnowing on glacial-interglacial timescales.

6. Conclusions

This paper presented sedimentation rates, density, and magnetic susceptibility for a suite of seven cores covering almost 700,000 years of sedimentation on the Juan de Fuca Ridge. Age models were generated from benthic $\delta^{18}O$ and subsequently refined using dry bulk density stratigraphy, resulting in a shared chronostratigraphy within the North Pacific. Spatial and temporal sedimentation patterns were presented to

Fig. 7. Backscatter amplitude map and profiles. (*Top*) Map of backscatter amplitudes across the JdFR region acquired with the shipboard EM122 multibeam sonar ranging from high backscatter amplitudes (orange) to low backscatter amplitudes (blue). Backscatter amplitude varies inversely with sediment thickness, so that the high backscatter on the axial plateau suggests a relatively thin sediment cover. Three north-south profiles passing through the core sites (black circles) are indicated with black lines. Ridge-perpendicular profiles are provided in Supplemental Figure 4. (*Bottom*) Three profiles of backscatter amplitude as defined in the map. Profiles correspond with crustal isochrons, so that A–A′ is on ~700 ka crust, B–B′ is on 1 Ma crust, and C–C′ is on 1.8 Ma crust. Bathymetry is shown in gray, with depth indicated on the right y-axis. Backscatter amplitude is shown in blue, with amplitude indicated on the left y-axis.

investigate how near-ridge sedimentary environments may have varied with glacial-interglacial cycles. Sedimentation rates generally range from 1 to 3 cm/kyr, with background pelagic sedimentation rates close to 1 cm/kyr, and they are spatially heterogeneous, likely reflecting sediment remobilization caused by the high relief and stronger bottom currents of the near-ridge environment. The primary mode of sedimentation is diverging sedimentation rates with distance from the ridge, reflecting the pervasiveness of localized sediment redistribution. The secondary mode of sedimentation is glacial-interglacial variation in sedimentation rates, reflecting carbonate preservation cycles or the susceptibility of fine material to remobilization and lateral transport along the seafloor.

Acknowledgements

The authors thank the captain and crew of the R/V Atlantis, the Oregon State University Coring group, and the staff of the LDEO Core Repository. The authors also thank Tanzhuo Liu, Kelly Luis, Tianjia Liu, Anna LoPresti, Christy Jenkins, Carly Peltier, and Wei Huang for assistance with $\delta^{18}O$ sample processing and analysis at LDEO, and Martin Fleisher for assistance with shipboard multi-sensor track analyses. Dr. Neil Mitchell, Dr. Mitchell Lyle, and one anonymous reviewer provided feedback that greatly improved the manuscript. The data are archived on the NOAA paleoclimate database. This research was funded by NSF-FESD award #AGS-1338832.

Appendix A. Supplementary data

Supplementary data to this article can be found online at http://dx.doi.org/10.1016/j.margeo.2016.08.003.

References

Baker, E.T., Lavelle, J.W., Feely, R.A., Massoth, G.J., Walker, S.L., Lupton, J.E., 1989. Episodic venting of hydrothermal fluids from the Juan de Fuca Ridge. J. Geophys. Res. 94, 9237–9250.
Beaulieu, S.E., 2002. Accumulation and fate of phytodetritus on the sea floor. Oceanogr. Mar. Biol. Annu. Rev. 40, 171–232.
Berger, W.H., 1979. Preservation of Foraminifera. In: Lipps, J.H. (Ed.), Foraminiferal Ecology and Paleoecology. Society of Economic Paleontologists & Mineralogists, Tulsa, OK, pp. 105–155.
Bloemendal, J., deMenocal, P.B., 1989. Evidence for a change in the periodicity of tropical climate cycles at 2.4 Myr from whole-core magnetic susceptibility measurements. Nature 342, 897–900.
Breitzke, M., 2006. Physical properties of marine sediments. In: Schulz, H.D., Zabel, M. (Eds.), Marine Geochemistry. Springer, Berlin Heidelberg, pp. 27–71.
Carbotte, S.M., Detrick, R.S., Harding, A., Canales, J.P., Babcock, J., Kent, G., Van Ark, E., Nedimovic, M., Diebold, J., 2006. Rift topography linked to magmatism at the intermediate spreading Juan de Fuca Ridge. Geology 34, 209–212.
Carbotte, S.M., Nedimović, M.R., Canales, J.P., Kent, G.M., Harding, A.J., Marjanović, M., 2008. Variable crustal structure along the Juan de Fuca Ridge: influence of on-axis hot spots and absolute plate motions. Geochem. Geophys. Geosyst. 9.
Carmichael, R.S., 1982. Magnetic properties of minerals and rocks. In: Carmichael, R.S. (Ed.), Handbook of Physical Properties of Rocks. CRC Press, Boca Raton, Florida, pp. 229–287.
Chappell, J., Shackleton, N.J., 1986. Oxygen isotopes and sea level. Nature 324, 137–140.
Davis, E.E., Karsten, J.L., 1986. On the cause of the asymmetric distribution of seamounts about the Juan de Fuca ridge: ridge-crest migration over a heterogeneous asthenosphere. Earth Planet. Sci. Lett. 79, 385–396.
deMenocal, P.B., Bloemendal, J., King, J., 1991. A rock magnetic record of monsoonal dust deposition to the Arabian Sea: evidence for a shift in the mode of deposition at 2.4 Ma. Proc. ODP Sci. Results 117, 389–407.
Dubois, N., Mitchell, N.C., 2012. Large-scale sediment redistribution on the equatorial Pacific seafloor. Deep-Res. I Oceanogr. Res. Pap. 69, 51–61.
Egbert, G.D., Ray, R.D., Bills, B.G., 2004. Numerical modeling of the global semidiurnal tide in the present day and in the last glacial maximum. J. Geophys. Res. 109, C03003.
Ewing, M., Ewing, J.I., Talwani, M., 1964. Sediment distribution in the oceans: the Mid-Atlantic Ridge. Geol. Soc. Am. Bull. 75, 17–36.
Farrell, J.W., Prell, W.L., 1989. Climatic change and $CaCO_3$ preservation: an 800,000 year bathymetric reconstruction from the Central Equatorial Pacific Ocean. Paleoceanography 4, 447–466.
Francois, R., Frank, M., Rutgers van der Loeff, M., Bacon, M.P., 2004. ^{230}Th normalization: an essential tool for interpreting sedimentary fluxes during the late Quaternary. Paleoceanography 19, PA1018.
Galbraith, E.D., Kienast, M., Jaccard, S.L., Pedersen, T.F., Brunelle, B.D., Sigman, D.M., Kiefer, T., 2008. Consistent relationship between global climate and surface nitrate utilization in the western subarctic Pacific throughout the last 500 ka. Paleoceanography 23, 1–11.
Goldfinger, C., Nelson, C.H., Morey, A.E., Johnson, J.E., Patton, J.R., Karabanov, E., Gutierrez-Pastor, J., Eriksson, A.T., Gracia, E., Dunhill, G., Enkin, R.J., Dallimore, A., Vallier, T., 2012. Turbidite event history — methods and implications for Holocene paleoseismicity of the Cascadia subduction zone. US Geol. Surv. Prof. Pap. 1661-F (170 pp.).
Gunn, D.E., Best, A.I., 1998. A new automated nondestructive system for high resolution multi-sensor core logging of open sediment cores. Geo-Mar. Lett. 18, 70–77.
Hauschild, J., Grevemeyer, I., Kaul, N., Villinger, H., 2003. Asymmetric sedimentation on young ocean floor at the East Pacific Rise, 15°S. Mar. Geol. 193, 49–59.
Heezen, B.C., Rawson, M., 1977. Visual observations of contemporary current erosion and tectonic deformation on the Cocos Ridge Crest. Mar. Geol. 23, 173–196.
Hickey, B.M., 1979. The California current system—hypotheses and facts. Prog. Oceanogr. 8, 191–279.
Horn, D.R., Ewing, M., Delach, M.N., Horn, B.M., 1971. Turbidites of the Northeast Pacific. Sedimentology 16, 55–69.
Jaccard, S.L., Haug, G.H., Sigman, D.M., Pedersen, T.F., Thierstein, H.R., Röhl, U., 2005. Glacial/interglacial changes in Subarctic North Pacific stratification. Science 308, 1003–1006.
Johnson, D.A., Johnson, T.C., 1970. Sediment redistribution by bottom currents in the central Pacific. Deep-Sea Res. 17, 157–169.
Karlin, R., Lyle, M.W., Zahn, R., 1992. Carbonate variations in the northeast Pacific during the late Quaternary. Paleoceanography 7, 43–61.
Karsten, J.L., Delaney, J.R., 1989. Hot spot-ridge crest convergence in the northeast Pacific. J. Geophys. Res. 94, 700–712.
Key, R.M., Quay, P.D., Schlosser, P., McNichol, A., von Reden, K., Schneider, R.J., Elder, K.L., Stuiver, M., Östlund, H.G., 2002. WOCE radiocarbon IV: Pacific Ocean results; P10, P13N, P14C, P18, P19 & S4P. Radiocarbon 44, 239–392.
Kienast, S.S., Kienast, M., Mix, A.C., Calvert, S.E., François, R., 2007. Thorium-230 normalized particle flux and sediment focusing in the Panama Basin region during the last 30,000 years. Paleoceanography 22.
Kroopnick, P.M., 1985. The distribution of ^{13}C of CO_2 in the world oceans. Deep-Sea Res. 32, 57–84.
Labeyrie, L.D., Duplessy, J.-C., Blanc, P.L., 1987. Variations in mode of formation and temperature of oceanic deep waters over the past 125,000 years. Nature 327, 477–482.
Lam, P.J., Robinson, L.F., Blusztajn, J., Li, C., Cook, M.S., McManus, J.F., Keigwin, L.D., 2013. Transient stratification as the cause of the North Pacific productivity spike during deglaciation. Nat. Geosci. 6, 622–626.
Larrasoaña, J.C., Roberts, A.P., Rohling, E.J., 2008. Magnetic susceptibility of eastern Mediterranean marine sediments as a proxy for Saharan dust supply? Mar. Geol. 254, 224–229.
Lavelle, J.W., 2012. On the dynamics of current jets trapped to the flanks of mid-ocean ridges. J. Geophys. Res. Oceans 117, 1–12.
Lavelle, J.W., Cannon, G.A., 2001. On subinertial oscillations trapped by the Juan de Fuca Ridge, northeast Pacific. J. Geophys. Res. 106, 31099.
Lisiecki, L.E., Raymo, M.E., 2005. A Pliocene-Pleistocene stack of 57 globally distributed benthic $d^{18}O$ records. Paleoceanography 20, PA1003.
Lister, C.R.B., 1976. Control of pelagic sediment distribution by internal waves of tidal period: possible interpretation of data from the southern East Pacific Rise. Mar. Geol. 20, 297–313.
Lonsdale, P., Normark, W.R., Newman, W.A., 1972. Sedimentation and erosion on Horizon Guyot. Geol. Soc. Am. Bull. 83, 289–316.
Macdonald, A.M., Mecking, S., Robbins, P.E., Toole, J.M., Johnson, G.C., Talley, L., Cook, M., Wijffels, S.E., 2009. The WOCE-era 3-D Pacific Ocean circulation and heat budget. Prog. Oceanogr. 82, 281–325.
Marcantonio, F., Lyle, M., Ibrahim, R., 2014. Particle sorting during sediment redistribution processes and the effect on ^{230}Th-normalized mass accumulation rates. Geophys. Res. Lett. 41, 5547–5554.
Marks, N.S., 1981. Sedimentation on new ocean crust: the Mid-Atlantic Ridge at 37°N. Mar. Geol. 43, 65–82.
Martinson, D.G., Pisias, N.G., Hays, J.D., Imbrie, J., Moore, T.C., Shackleton, N.J., 1987. Age dating and the orbital theory of the ice ages: development of a high-resolution 0 to 300,000 year chronostratigraphy. Quat. Res. 27, 1–29.
Massoth, G.J., Baker, E.T., Lupton, J.E., Feely, R.A., Butterfield, D.A., Von Damm, K.L., Roe, K.K., Lebon, G.T., 1994. Temporal and spatial variability of hydrothermal manganese and iron at Cleft segment, Juan de Fuca Ridge. J. Geophys. Res. 99, 4905–4923.
Mayer, L.A., 1979. Deep sea carbonates: acoustic, physical, and stratigraphic properties. J. Sediment. Res. 49, 819–836.
Mayer, L.A., 1991. Extraction of high-resolution carbonate data for palaeoclimate reconstruction. Nature 352, 148–150.
Mitchell, N.C., 1993. A model for attenuation of backscatter due to sediment accumulations and its application to determine sediment thicknesses with GLORIA sidescan sonar. J. Geophys. Res. 98, 22477–22493.
Mitchell, N.C., 1995. Diffusion transport model for pelagic sediments on the Mid-Atlantic Ridge. J. Geophys. Res. 100, 19991–20009.
Mitchell, N.C., Lee, S.V., 1998. Sediment accumulation rates from Deep Tow profiler records and DSDP Leg 70 cores over the Galapagos spreading centre. In: Cramp, A., MacLeod, C.J., Jones, E.J.W. (Eds.), Geological Evolution of Ocean Basins: Results From the Ocean Drilling Program. Geological Society, London, pp. 199–209.
Mitchell, N.C., Huthnance, J.M., 2013. Geomorphological and geochemical evidence (^{230}Th anomalies) for cross-equatorial currents in the central Pacific. Deep-Sea Res. I Oceanogr. Res. Pap. 78, 24–41.
Mitchell, N.C., Allerton, S., Escartín, J., 1998. Sedimentation on young ocean floor at the Mid-Atlantic Ridge, 29°N. Mar. Geol. 148, 1–8.
Mitchener, H., Torfs, H., 1996. Erosion of mud/sand mixtures. Coast. Eng. 29, 1–25.

Normark, W.R., Morton, J.L., Koski, R.A., Clague, D.A., Delaney, J.R., 1983. Active hydrothermal vents and sulfide deposits on the southern Juan de Fuca Ridge. Geology 11, 158.
Polzin, K.L., 1997. Spatial variability of turbulent mixing in the abyssal ocean. Science 276, 93–96.
Prell, W.L., Imbrie, J., Martinson, D.G., Morley, J.J., Pisias, N.G., Shackleton, N.J., Streeter, H.F., 1986. Graphic correlation of oxygen isotope stratigraphy application to the Late Quaternary. Paleoceanography 1, 137–162.
Reimer, P.J., Bard, E., Bayliss, A., Beck, J.W., Blackwell, P.G., Ramsey, C.B., Buck, C.E., Cheng, H., Edwards, R.L., Friedrich, M., Grootes, P.M., Guilderson, T.P., Haflidason, H., Hajdas, I., Hatte, C., Heaton, T.J., Hoffman, D.L., Hogg, A.G., Hughen, K.A., Kaiser, K.F., Kromer, B., Manning, S.W., Niu, M., Reimer, R.W., Richards, D.A., Scott, E.M., Southon, J.R., Staff, R.A., Turney, C.S.M., van der Plicht, J., 2013. Intcal13 and Marine13 radiocarbon age calibration curves 0–50,000 years calBP. Radiocarbon 55, 1869–1887.
Ruddiman, W.F., 1972. Sediment redistribution on the Reykjanes Ridge: seismic evidence. Geol. Soc. Am. Bull. 83, 2039–2062.
Schrag, D.P., Hampt, G., Murray, D.W., 1996. Pore fluid constraints on the temperature and oxygen isotopic composition of the glacial ocean. Science 272, 1930–1932.
Stuiver, M., Reimer, P.J., 1993. Extended ^{14}C database and revised Calib 3.0 ^{14}C age calibration program. Radiocarbon 35, 215–230.
Thomson, R.E., Mihaly, S.F., Rabinovich, A.B., McDuff, R.E., Veirs, S.R., Stahr, F.R., 2003. Constrained circulation at Endeavour ridge facilitates colonization by vent larvae. Nature 424, 545–549.
Thurnherr, A.M., Speer, K.G., 2003. Boundary mixing and topographic blocking on the Mid-Atlantic Ridge in the South Atlantic. J. Phys. Oceanogr. 33, 848–862.
Thurnherr, A.M., St. Laurent, L.C., Speer, K.G., Toole, J.M., Ledwell, J.R., 2005. Mixing associated with sills in a canyon on the midocean ridge flank. J. Phys. Oceanogr. 35, 1370–1381.
Turnewitsch, R., Reyss, J.-L., Chapman, D.C., Thomson, J., Lampitt, R.S., 2004. Evidence for a sedimentary fingerprint of an asymmetric flow field surrounding a short seamount. Earth Planet. Sci. Lett. 222, 1023–1036.
Turnewitsch, R., Reyss, J., Nycander, J., Waniek, J.J., Lampitt, R.S., 2008. Internal tides and sediment dynamics in the deep sea — evidence from radioactive ^{234}Th/^{238}U disequilibria. Deep-Sea Res. I 55, 1727–1747.
Turnewitsch, R., Falahat, S., Nycander, J., Dale, A., Scott, R.B., Furnival, D., 2013. Deep-sea fluid and sediment dynamics-influence of hill- to seamount-scale seafloor topography. Earth-Sci. Rev. 127, 203–241.
van Andel, T., Komar, P.D., 1969. Ponded sediments of the Mid-Atlantic Ridge between 22° and 23° north latitude. Geol. Soc. Am. Bull. 1163–1190.
von Stackelberg, U., von Rad, U., Zobel, B., 1979. Asymmetric sedimentation around Great Meteor Seamount (North Atlantic). Mar. Geol. 33, 117–132.
Webb, H.F., Jordan, T.H., 2001. Pelagic sedimentation on rough topography 1. Forward model. J. Geophys. Res. 106, 30433–30449.
Wilson, D.S., 1993. Confidence intervals for motion and deformation of the Juan de Fuca plate. J. Geophys. Res. 98, 16053–16071.